Research Article | Vol. 24, No. 24 | 28 Nov 2016 | OPTICS EXPRESS 27160

Optics EXPRESS

Polarization-variable emitter for terahertz time-domain spectroscopy

DMITRY S. BULGAREVICH,[1,2,*] MAKOTO WATANABE,[1] MITSUHARU SHIWA,[1] GUDRUN NIEHUES,[2,3] HIDEAKI KITAHARA,[2] AND MASAHIKO TANI[4]

[1]*National Institute for Materials Science, 1-2-1 Sengen, Tsukuba, Ibaraki 305-0047, Japan*
[2]*Research Center for Development of Far-Infrared Region, University of Fukui, 3-9-1 Bunkyo, Fukui 910-8507, Japan*
[3]*Laboratory for Applications of Synchrotron Radiation, Karlsruhe Institute of Technology, 76131 Karlsruhe, Germany*
[4]*tani@fir.u-fukui.ac.jp*
[*]*DMITRY.Bulgarevich@nims.go.jp*

Abstract: We report on the progress in the development of linear polarization-variable multi-electrode emitters for terahertz time-domain spectroscopy. The results on its microfabrication, the finite element method modeling of appropriate bias distribution between electrodes, the finite-difference time-domain simulated spectral output, and actual experimental testing are presented. The rotation of the emitted terahertz field with linear polarization on an angle multiple of 45° can be achieved by synchronized bias and single polarizer rotations.

OCIS codes: (300.6495) Spectroscopy, terahertz; (230.5440) Polarization-selective devices; (230.4000) Microstructure fabrication; (000.4430) Numerical approximation and analysis.

References and links

1. E. Castro-Camus and M. B. Johnston, "Extraction of the anisotropic dielectric properties of materials from polarization-resolved terahertz time-domain spectra," J. Opt. A, Pure Appl. Opt. **11**(10), 105206 (2009).
2. T. Nagashima, M. Tani, and M. Hangyo, "Polarization-sensitive THz-TDS and its application to anisotropy sensing," J. Infrared Milli. **34**(11), 740–775 (2013).
3. E. Castro-Camus, "Polarization-resolved terahertz time-domain spectroscopy," J. Infrared Milli. **33**(4), 418–430 (2012).
4. H. Dong, Y. Gong, V. Paulose, and M. Hong, "Polarization state and Mueller matrix measurements in terahertz-time domain spectroscopy," Opt. Commun. **282**(18), 3671–3675 (2009).
5. T. Tanabe, K. Watanabe, Y. Oyama, and K. Seo, "Polarization sensitive THz absorption spectroscopy for the evaluation of uniaxially deformed ultra-high molecular weight polyethylene," NDT Int. **43**(4), 329–333 (2010).
6. D. S. Bulgarevich, M. Shiwa, G. Niehues, and M. Tani, "Linear dichroism detection and analysis in terahertz spectral range," IEEE Trans. Terahertz Sci. Technol. **5**(6), 1097–1099 (2015).
7. K. Wiesauer and C. Jördens, "Recent advances in birefringence studies at THz frequencies," J. Infrared Milli. **34**(11), 663–681 (2013).
8. Y. Kim, J. Ahn, B. G. Kim, and D.-S. Yee, "Terahertz birefringence in zinc oxide," Jpn. J. Appl. Phys. **50**(3R), 030203 (2011).
9. M. Neshat and N. P. Armitage, "Developments in THz range ellipsometry," J. Infrared Milli. **34**(11), 682–708 (2013).
10. J. V. Rudd, J. L. Johnson, and D. M. Mittleman, "Quadrupole radiation from terahertz dipole antennas," Opt. Lett. **25**(20), 1556–1558 (2000).
11. H. Park, E. P. J. Parrott, Z. Huang, H. P. Chan, and E. Pickwell-MacPherson, "Accurate photoconductive antenna characterization using a thin film polarizer," Appl. Phys. Lett. **101**(12), 121108 (2012).
12. D. S. Bulgarevich, M. Watanabe, M. Shiwa, G. Niehues, S. Nishizawa, and M. Tani, "A polarization-sensitive 4-contact detector for terahertz time-domain spectroscopy," Opt. Express **22**(9), 10332–10340 (2014).
13. G. Niehues, S. Funkner, D. S. Bulgarevich, S. Tsuzuki, T. Furuya, K. Yamamoto, M. Shiwa, and M. Tani, "A matter of symmetry: terahertz polarization detection properties of a multi-contact photoconductive antenna evaluated by a response matrix analysis," Opt. Express **23**(12), 16184–16195 (2015).
14. Y. Hirota, R. Hattori, M. Tani, and M. Hangyo, "Polarization modulation of terahertz electromagnetic radiation by four-contact photoconductive antenna," Opt. Express **14**(10), 4486–4493 (2006).
15. H. Suo, K. Takano, S. Ohno, H. Kurosawa, K. Nakayama, T. Ishihara, and M. Hangyo, "Polarization property of terahertz wave emission from gammadion-type photoconductive antennas," Appl. Phys. Lett. **103**(11), 111106 (2013).

#273521 http://dx.doi.org/10.1364/OE.24.027160
Journal © 2016 Received 6 Sep 2016; revised 19 Oct 2016; accepted 19 Oct 2016; published 14 Nov 2016

Optics EXPRESS

16. S. Winnerl, B. Zimmermann, F. Peter, H. Schneider, and M. Helm, "Terahertz Bessel-Gauss beams of radial and azimuthal polarization from microstructured photoconductive antennas," Opt. Express **17**(3), 1571–1576 (2009).
17. J. A. Deibel, M. D. Escarra, and D. M. Mittleman, "Photoconductive terahertz antenna with radial symmetry," Electron. Lett. **41**(5), 226–228 (2005).
18. J. A. Deibel, K. Wang, M. Escarra, N. Berndsen, and D. M. Mittleman, "The excitation and emission of terahertz surface plasmon polaritons on metal wire waveguides," C. R. Phys. **9**(2), 215–231 (2008).
19. D. S. Bulgarevich, M. Watanabe, and M. Shiwa, 2015 Japan Patent Pending 15-MS-055.
20. H. Makabe, Y. Hirota, M. Tani, and M. Hangyo, "Polarization state measurement of terahertz electromagnetic radiation by three-contact photoconductive antenna," Opt. Express **15**(18), 11650–11657 (2007).
21. V. Siklitsky and A. Tolmatchev, "Physical Properties of Semiconductors," *http://www.ioffe.ru/SVA/NSM/*.

1. Introduction

The development of polarization-sensitive terahertz (THz) time-domain spectroscopy (TDS) is important for non-destructive testing (NDT) of materials, which are opaque in UV/Vis and IR spectral regions, but having the optical anisotropy properties in THz range [1–4]. For example, the production, stress, and damage induced linear dichroism [5,6], birefringence [7,8], or ellipticity [2,9] can be used to understand the quality and state of pure polymers, their composites, crystals, or dielectric and semiconductor materials. The THz-TDS also has additional advantages such as non-ionizing and harmless nature, the ability to operate at ambient conditions, and to provide the rich information on materials dielectric properties.

In typical THz-TDS scheme for optical anisotropy detection [6], a pair of THz photoconductive dipole emitter/detector (DE/DD) antennas and three rotatable wire-grid polarizers (P_n) are employed. It allows the registrations of only the sample-modified polarization components. However, the main disadvantages of this and similar setups are the fixed angles for maximum DE/DD linear polarization output/sensitivity [10,11] and deterioration of signal-to-noise ratio (SNR) at some polarizer angles with respect to DE/DD electrodes by Malu's law. As such, the polarization-variable THz emitters and polarization-sensitive THz detectors are very desirable for NDT applications based on optical anisotropy analysis. Regarding THz-TDS detectors, several multi-contact ones have been previously reviewed [2,3] and recently reported [12,13]. For example, our detector has a good linear angular response similar to an ideal one [12,13]. As for corresponding emitters, our previously reported four-contact one was able to produce the alternated ± 45° linear polarization output with slight polarization distortion and ellipticity (–0.05 to + 0.1) due to spatial inhomogeneity of the photoelectric property in the photoconductive substrate, the inhomogeneous distribution in the pump beam intensity, and the deviation of the bias field distribution from the ideal symmetry (imperfect patterning of the contact electrodes) [14]. The emitters with fixed elliptical [15], azimuthal [16], and radial [17,18] polarization ones had been also designed and tested.

In this work, we present our additional attempts on microfabrication and performance improvements for multi-electrode emitter, which was redesigned to generate and rotate in a stepwise manner (45° steps, 360° rotation) the linear polarization component of the broadband THz field by appropriate DC bias distribution between its electrodes. Our approach also opens the route to design and realize other sophisticated polarization outputs with photoconductive antennas.

2. Experimental

The 8-contact emitter (8-CE) for polarization-variable THz-TDS was microfabricated as reported in [12,19]. Figures 1(a)-1(e) show its photomask design, actual photos, and optical scheme of testing. As shown in Fig. 1(c), the trenches of 0.5 μm wide and 1.5 μm deep were focused ion beam (FIB) etched in a low-temperature-grown gallium arsenide (LT-GaAs) substrate to increase the antenna breakdown voltage between neighboring electrodes, i.e. to improve its robustness. It also decreases the parasitic currents generated by the scattered laser light between such electrodes. The details of the THz-TDS setup were described in an earlier

Optics EXPRESS

work [20]. The pump/probe laser pulses on DE or 8-CE and DD antennas were modulated at 2 kHz with an optical chopper. The Thorlabs C330TME-B objectives with 0.68 numerical apertures were used for pump/probe beam focusing between antenna electrodes. With IR camera and PC monitor, they were also utilized to observe and adjust the laser spot position from reflected laser light.

Without polarizers, the spatial alignment of dipole electrodes in DE/DD pair was initially adjusted for maximum THz signal. Then, polarizer (P) and analyzer (A) were placed and rotated between DE and DD for maximum transmission (T). These P and A installations at azimuthal angles θ_1 and θ_2 are set to be 0°, respectively. After that, the DE was replaced on 8-CE [see Fig. 1(e)]. Its polarization output was studied by rotating of P at fixed A ($\theta_2 = 0°$). Experimentally, the multichannel Interface PCI-3346A board for DC output and in-house developed software were used for appropriate bias application and rotation on mounted and wired 8-CE antenna chip [see Fig. 1(d)].

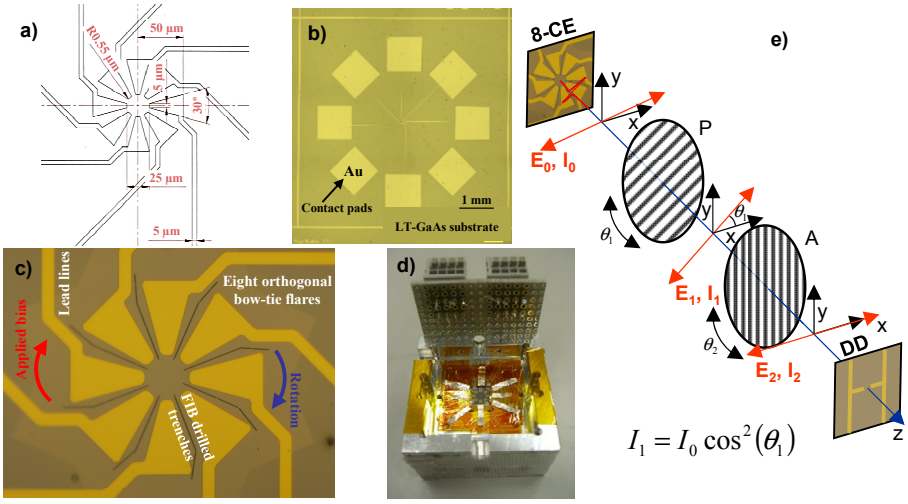

Fig. 1. Microfabricated 8-CE (a)-(d) and scheme of its testing (e): the photomask geometry in mm (a); the total view of the microfabricated bow-tie electrodes, lead lines, and 1 × 1 mm contact pads (b); the magnified detector center with ~50 μm bowie-tie flares (c); the 8-CE chip mounted on Si lens and wired to terminals for DC bias application (d); antenna; optical scheme of testing with wire-grid polarizers (e).

The finite-difference time-domain (FDTD) and finite-element mesh (FEM) methods were used to model the 8-CE spectral output and appropriate DC bias distribution between antenna electrodes. For these purposes, the FDTD Solutions and DEVICE solvers (Lumerical Solutions, Inc.) were applied, respectively. Since emitter radiation and receiving patterns are reciprocal, the 8-CE spectral output was FDTD modeled for two opposite electrodes in detector configuration. The actual electrode image after microfabrication was used as an input geometry in these simulations. The total simulation volume was 2100 × 2100 × 200 μm^3 and the minimum mesh dimensions around antenna center (30 × 10 μm^2 area) were 0.02 × 0.02 μm^2 in order to model correctly the geometrical features of electrode tips. Other details were similar to reported ones [12]. The FEM electrostatic 3D modeling was conducted with the Gummel's solver in DC mode, the global mesh constrains between 0.02 and 1 μm for 60 × 60 × 10 μm^3 simulation volume, and with photomask geometry of electrodes and FIB trenches on LT-GaAs substrate. In DEVICE solver, the DC bias sweepings on electrodes were conducted between 0 and 3 V with 0.05 V interval.

Optics EXPRESS

3. Results and discussion

Figure 2 shows the example of the FEM modeling of static electric field (E) distribution between 8-CE electrodes with optimized DC bias application. Such optimization was necessary in order to reduce the parasitic photocurrents between multiple electrodes for generation of the linearly polarized THz emission. The best modeling results were considered when largest and more symmetrical area with $E_x \gg E_y$ was formed at the antenna center for E components along x and y axes. As shown in Fig. 2, such area with E_x / E_y = 10^2-10^3 can be obtained by using the particular bias distribution on antenna electrodes. The white circle in Fig. 2 corresponds to the spot size of the focused laser beam achievable with our optics. Consequently, the photo-generated carriers in LT-GaAs substrate with such DC bias distribution will mainly flow between 1st and 5th electrodes by focusing the pump laser beam into antenna center. This photocurrent direction and antenna electrode geometry determine the polarization nature of the emitted THz waves. The photocurrent direction with bias distribution in Fig. 2 corresponds to its rotation angle β = 0° with respect to x -axis. Then, by rotating of such bias distribution on β incremental of 45°, the 8-CE output polarization also could be rotated accordingly. Here it should be also mentioned that maximum value of calculated static E was below the breakdown field for GaAs [21] at DC bias setup in Fig. 2.

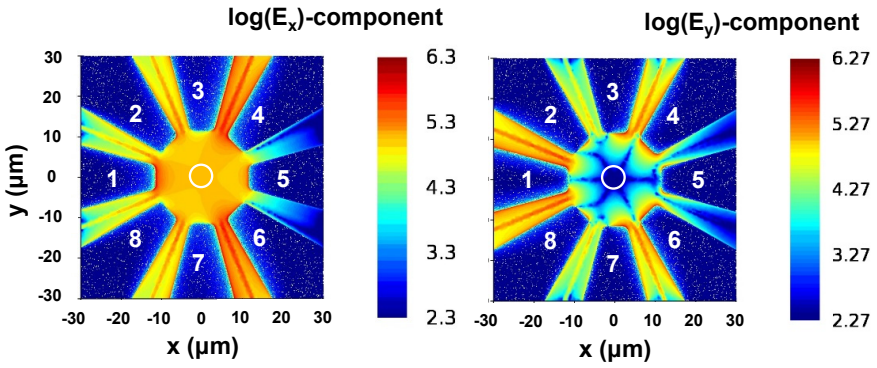

Fig. 2. FEM simulation results of static E distribution at the center of 8-CE between DC-biased antenna electrodes for E_x and E_y components (in V/m): 2.9 V at 1st, 1.7 V at 2nd and 8th, 1.4 V at 3rd and 7th and 0 V at 4th, 5th, and 6th electrodes.

Figures 3(a) and 3(b) display the experimental and FDTD modeling results for 8-CE. The experimental THz spectra where obtained by collecting the E_x component of THz field with DD at different θ_1, θ_2, and β angles for polarizer and bias setups, respectively. As shown in Fig. 1(e), the DD is mainly sensitive to such component of incoming THz wave due to its geometrical nature. As the result, two spectrally different and spatially orthogonal components from 8-CE radiation can be identified by registering the E_x spectral responses for β = 0° and β = –90° biases with θ_1 = θ_2 = 0° for P and A [see the corresponding black and lime spectra in Fig. 3(a)]. In other words, DD registered strong E_x-component in 8-CE radiation even at β = –90°. Therefore, 8-CE generates E_x and parasitic E_y components at β = 0°. More accurately, the $E_y = \sqrt{2}E_{x,-45°} - E_x$ was calculated and

Optics EXPRESS

plotted in Fig. 3(a) from measurements of E_x at $\theta_1 = \theta_2 = \beta = 0°$ and $E_{x,-45°}$ at $\theta_1 = -45°$, $\theta_2 = \beta = 0°$ setups (see black and blue spectra).

These E_x and E_y components from 8-CE contain the higher and lower frequency resonances of bow-tie and lead line electrodes at ~0.35 THz and ~0.12 THz, respectively (see black-colored solid and dashed line spectra). Their spectral positions are determined by the corresponding parts of the electrode lengths and LT-GaAs refractive index. Regarding E_x component, the experimental 8-CE spectra registered with DD ($\theta_1 = \theta_2 = \beta = 0°$) agree reasonably well with FDTD simulations. This can be seen by comparing the experimental DE/DD spectral signature (orange-colored dashed line spectrum) with FDTD estimated E_x component (red-colored solid line spectrum) and by taking into account the experimental spectral distortions due to the water vapor lines as well as the DE/DD spectral convolution. From inserts in Fig. 3(a), it can be also seen that complete suppression of parasitic E_y resonance is not possible even for orthogonal design of lead lines with respect to bowie-tie flares (see the standing waves on lead lines).

In time domain, the experimental E_x (lime color) and E_y (blue color) components as well as reconstructed total E (red color) trajectory for 8-CE THz radiation are presented in Fig. 3(b) as a 3D plot. Besides such E_x, E_y, and E waveforms, the projection (cyan color) of E onto the E_xE_y-plane is also shown. It clearly demonstrates the nonlinear polarization nature of the 8-CE THz radiation.

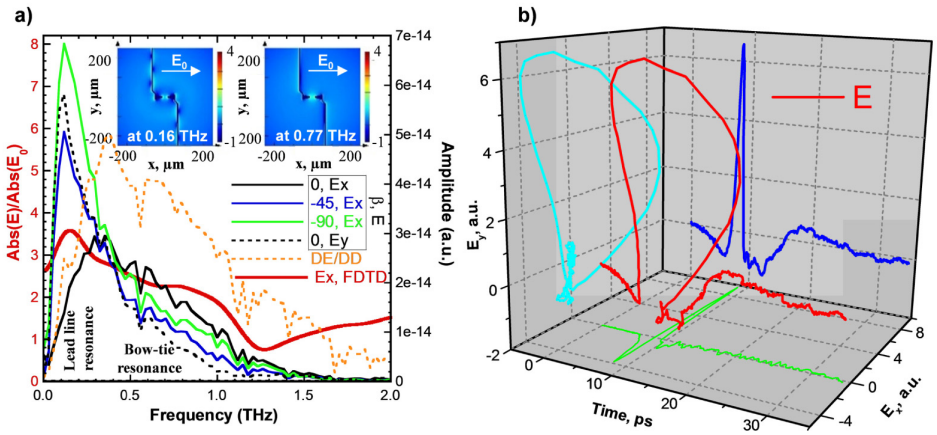

Fig. 3. Experimental and FDTD modeled data for 8-CE in frequency (a) and time domains (b). The comparison between FDTD simulation of 8-CE spectral signature, distribution of THz E_x-field between two opposite electrodes ($log\left(|E_x|^2 / |E_0|^2\right)$ color scales on inserts), and experimental spectral results (a). The experimental waveforms (b). The red and black y-axes in (a) are for FDTD and experimental results, respectively. The spectrum for DE/DD antennas in (a) is one-tenth amplitude of the actual one. The E_0 in (a) is the incident THz field amplitude in FDTD simulations. See text for more details.

Therefore, in order to extract and rotate the linear polarization of bow-tie component, the corresponding synchronized bias and P rotations can be used [see Fig. 4]. This proposed optical scheme avoids the S/N deteriorations with θ_1 increase, which are unavoidable by

Optics EXPRESS

using the typical dipole emitter and wire-grid polarizer setups even with multi-contact polarization-sensitive detectors due to the Malus's law. Compared to our previously reported 4-electrode emitter [14], we have an ability to rotate the linear polarization output in full 360° due to its 8-fold rotational symmetry, to change the emitter resonances frequency at the microfabrication stage with bow-tie flare length, and to have more flexible/tunable way to apply various bias distributions on its electrodes.

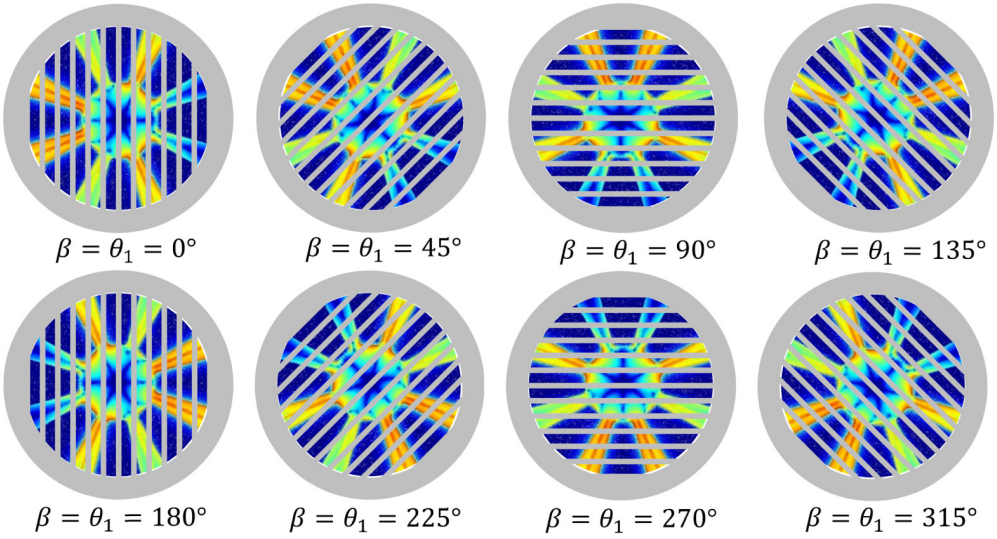

Fig. 4. The scheme of synchronized rotation of DC bias on 8-CE electrodes and *P* in front of 8-CE to achieve the linear polarization rotation of THz emission with constant intensity (see text for used notations).

4. Conclusion

Additional improvements and developments could be in the lead line geometry, microfabrication, LT-GaAs performance, optical alignments, and in combination of polarization-variable emitter with polarization-sensitive THz detector. The later topic is interesting for construction of linear dichroism spectrometer in THz range for NDT applications with optical anisotropy detection. In principle, the THz polarization outputs for our 8-CE are not limited to linear polarization with DC bias application. By appropriate distributions of AC bias values and phases on antenna electrodes, other polarization properties are also achievable. For this purpose, additional simulations and electronics for bias distribution will be necessary. For example, the elliptical or circular polarization outputs with 8-CE emitter will require the orthogonal photocurrents with 90° phase shift and with unequal or equal strength, respectively, within the spot of the pump laser beam at the multi-electrode antenna gap.

Funding

The Collaborative Research Funding from Research Center for Development of Far-Infrared Region of the University of Fukui (H26 FIRDM020B and H27 FIRDM002A).

Acknowledgments

The microfabrication was supported by WPI Research Center, MEXT, Japan. GN gratefully acknowledges the Japan Society for the Promotion of Science (JSPS) and the Alexander von Humboldt Foundation for supporting her work through a postdoctoral fellowship.